INTERNATIONAL GEOLOGY REVIEW, 2018
https://doi.org/10.1080/00206814.2018.1425922

Taylor & Francis
Taylor & Francis Group

ARTICLE

Asymmetry in oceanic crustal structure of the South China Sea basin and its implications on mantle geodynamics

Fan Zhang[a], Jian Lin[b], Xubo Zhang[b,c], Weiwei Ding[d], Tingting Wang[c] and Jian Zhu[b]

[a]Department of Ocean Science & Engineering, Southern University of Science and Technology, Shenzhen, China; [b]Department of Geology & Geophysics, Woods Hole Oceanographic Institution, Woods Hole, MA, USA; [c]State Key Laboratory of Marine Geology, School of Ocean and Earth Sciences, Tongji University, Shanghai, China; [d]The Second Institute of Oceanography, State Oceanic Administration, Hangzhou, China

ABSTRACT

We investigated the oceanic crustal structure and lithospheric dynamics of the South China Sea (SCS) basin through a comprehensive analysis of residual gravity anomaly and bathymetry combined with seismic constraints and interpretation from geodynamic modelling. We first calculated the residual mantle Bouguer anomaly (RMBA) of the oceanic crustal regions of the SCS by removing from free-air gravity anomaly the predicted gravitational attractions of water-sediment, sediment-crust, and crust-mantle interfaces, as well as the effects of lithospheric plate cooling, using the latest crustal age constraints including IODP Expedition 349 and recent deep-tow magnetic surveys. We then calculated models of the gravity-derived crustal thickness and calibrated them using the available seismic refraction profiles of the SCS. The gravity-derived crustal thickness models correlate positively with seismically determined crustal thickness values. Our analysis revealed that the isochron-averaged RMBA are consistently more negative over the northern flank of the SCS basin than the southern conjugate for magnetic anomaly chrons C8n (~25.18 Ma) to C5Dn (~17.38 Ma), implying warmer mantle and/or thicker crust over much of the northern flank. Computational geodynamic modelling yielded the following interpretations: (1) Models of asymmetric and variable spreading rates based on the relatively high-resolution deep-tow magnetic analysis would predict alternating thicker and thinner crust at the northern flank than the southern conjugate, which is inconsistent with the observed systematically thicker crust on the northern flank. (2) Models of episodic southward ridge jumps could reproduce the observed N-S asymmetry, but only for crustal age of 23.6–20 Ma. (3) Southward migration of the SCS ridge axis would predict slightly thinner crust at the northern flank, which is inconsistent with the observations. (4) Models of higher mantle temperatures of up to 25–50°C or >2% less depleted mantle sources on the northern flank could produce large enough anomalies to explain the observed N-S asymmetries.

ARTICLE HISTORY
Received 9 October 2017
Accepted 6 January 2018

KEYWORDS
South China Sea; gravity anomaly; oceanic crustal thickness; North-south asymmetry; mantle geodynamics

1. Introduction

The South China Sea (SCS) is located at the junction of the Eurasian, Philippine, and Indo-Australian plates and is one of the largest marginal seas in the west Pacific (Figure 1(a)). Despite its relatively short history of evolution, the SCS has experienced almost a complete Wilson cycle (Wilson 1966) from continental rifting and breakup to seafloor spreading, and then to subduction. The specific geological setting and unique evolutionary history make the SCS an ideal natural laboratory for investigating a variety of important scientific problems.

The SCS can be roughly divided into the northern continental margin, the southern continental margin, and the oceanic basin. It is generally accepted that the oceanic crust in the SCS basin was formed by seafloor spreading during the late Oligocene to mid-Miocene (Taylor and Hayes 1980, 1983; Briais *et al*. 1993; Li *et al*. 2015). Extensive geological and geophysical surveys have been carried out over the SCS, including the crustal and shallow mantle seismic surveys (e.g. Qiu *et al*. 2001; Yan *et al*. 2001; Hayes and Nissen 2005; Wang *et al*. 2006; Zhao *et al*. 2010; Ding *et al*. 2016). Based on analysis of magnetic anomaly data, Taylor and Hayes (1980, 1983) proposed that seafloor spreading in the East Sub-basin took place during 32–17 Ma, and this was modified to 30–16 Ma according to the timescales of Gradstein *et al*. (1993) and Cande and Kent (1995). Briais *et al*. (1993) suggested that seafloor spreading began at ~30 Ma in the Northwest and East Sub-basins, and then propagated into the Southwest Sub-basin after ~23.6 Ma (Ding and Li 2016), accompanied by a southward ridge jump (Xu *et al*. 2011). Based on the

CONTACT Jian Lin jlin@whoi.edu Department of Geology & Geophysics, Woods Hole Oceanographic Institution, Woods Hole, MA 02543, USA
Supplemental data for this article can be accessed here.

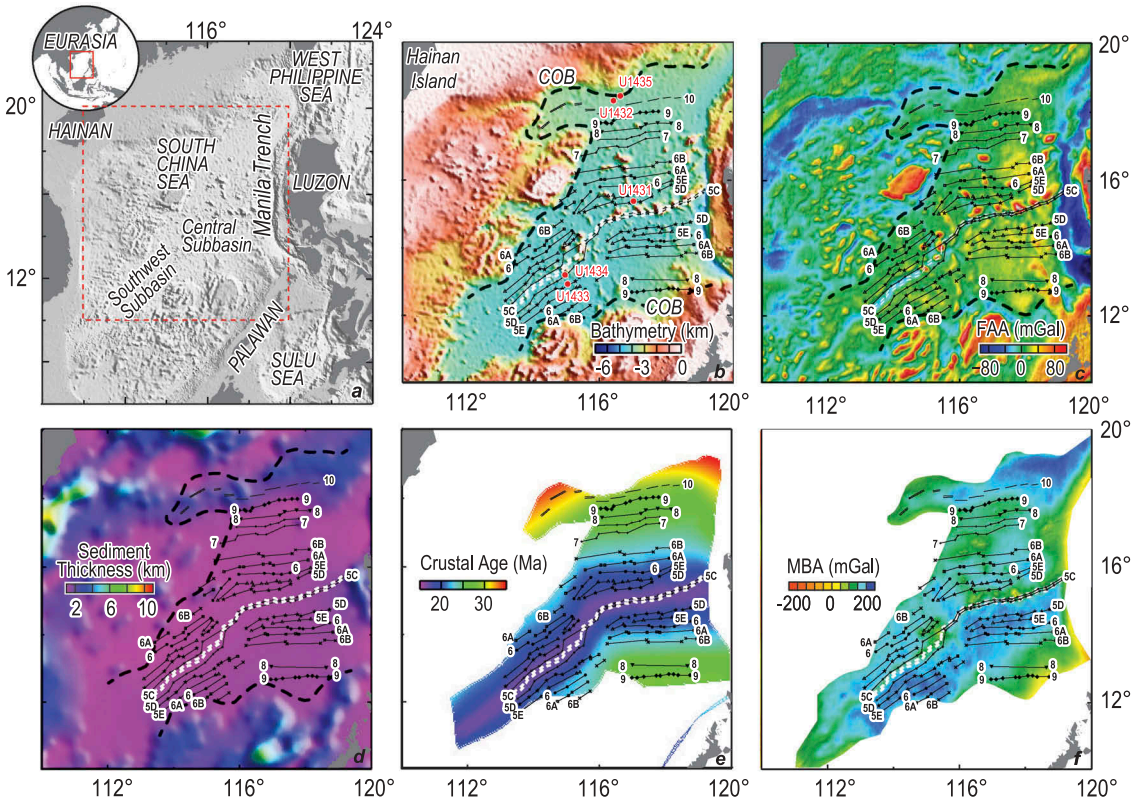

Figure 1. (a) Tectonic framework of the South China Sea (SCS). (b) Bathymetry (Smith and Sandwell 1997). Black lines mark the isochrones of the SCS basin (Briais *et al*. 1993). Red dots mark the sites of IODP Expedition 349. Double white dashed line marks the locations of fossile ridges. (c) Satellite-derived free air anomaly (FAA, Sandwell *et al*. 2014). (d) Sediment thickness (Divins 2003; Yang. *et al*. 2015). (e) Oceanic crustal age (Müller *et al*. 2008). (f) Calculated mantle Bouguer anomaly (MBA). The MBA was calculated by subtracting from FAA the predicted gravity effects of the water-sediment, sediment-crust, and crust-mantle interfaces for a reference crustal thickness of 5.5 km. Densities of water, crust, and mantle were assumed to be 1.03, 2.7, and 3.3 × 10^3 kg/m^3, respectively. The sediment was divided into six sub-layers of increasing density with depth (Wang *et al*).

ocean drilling results of IODP Expedition 349 (Koppers 2014; Li *et al*. 2015), as well as the deep-tow magnetic anomaly data (Li *et al*. 2014), the opening and cessation ages of the SCS are ~33 and ~15 Ma for the East Sub-basin, respectively. For the Southwest Sub-basin, the opening and cessation ages are about ~23 and 16–17 Ma (Li *et al*. 2015), respectively. These new results provided critical constraints on the opening scenario of the SCS. Seismic surveys of the SCS, however, are still limited only to a few relatively small patches within the vast SCS sub-basins. Earlier studies have investigated the basin-scale variations in the crustal structure of the SCS (e.g. Ludwig *et al*. 1979; Taylor and Hayes 1983; Liu *et al*. 1985; Chen and Lei 1987; Trung *et al*. 2004; Braitenberg *et al*. 2006; Li *et al*. 2012). There is a need to re-examine this basin-scale variability using the most updated information and to advance understanding of the mantle geodynamic processes.

The SCS spreading process showed important north-south asymmetries: (1) While various studies have calculated somewhat different models of the SCS spreading rates (e.g. Li and Song 2012; Song and Li 2012), the most updated model based on the relatively high-resolution deep-tow magnetic surveys revealed that relative to the southern conjugate, the northern flank was associated with faster spreading rates during ~33–25 Ma, slower rates during ~25–22 Ma, and similar rates at ~22–15 Ma (Li *et al*. 2014). (2) At the SCS East Sub-basin, the ridge axis jumped southward at about 23.8 Ma (Briais *et al*. 1993; Xu *et al*. 2011; Li *et al*. 2015). (3) Relative to the Eurasian plate, the SCS ridge axis migrated southward during the entire spreading period of 33–15 Ma (Li *et al*. 2015). (4) Distribution of seamounts is asymmetric in the SCS, with most seamounts located in the northern sub-basins (Wang *et al*. 2009). (5) It was proposed that the Hainan mantle plume might have affected the mantle beneath the northern SCS (Flower *et al*. 1992; Yan 2007; Yan *et al*. 2008, 2015; Xu *et al*. 2012; Huang *et al*. 2016; Wei *et al*., 2016; Xia *et al*. 2016). However, the detailed specific effects of the Hainan plume on the crustal structure and upper mantle temperature and compositions are still little known.

In this study, we used the most updated bathymetry, ship-borne and satellite-derived gravity, sediment thickness, and crustal age to calculate the gravity-derived and seismically calibrated oceanic crustal thickness distribution through the entire SCS ocean basin, and thereby investigate the characteristics of the SCS melt anomalies and mantle dynamics. We further conducted a series of geodynamic models to quantify the potential contributions to the observed north-south asymmetry in gravity and crustal structure considering the physical mechanisms of (1) N-S asymmetric and variable spreading rates; (2) southward ridge jump, (3) southward ridge migration, (4) asymmetry in mantle temperature, and (5) asymmetry in the mantle sources with varying degree of mantle depletion.

2. Data analysis

2.1 Data

Four primary datasets were used in the calculation of this study: Seafloor bathymetry (Figure 1(b)), shipboard and satellite-derived free-air gravity (Figure 1(c)), sediment thickness (Figure 1(d)), and crustal age based on magnetic anomaly (Figure 1(e)).

2.1.1. Bathymetry

The bathymetric data used in this study were extracted as 1-minute grid (Figure 1(b)) from the Global Topography dataset (V17.1; Smith and Sandwell 1997, http://topex.ucsd.edu/WWW_html/mar_topo.html), which is a combination of ship track measurements and satellite altimetry-derived topography. Much of the shipboard bathymetry measurements were already incorporated in the global bathymetry dataset, as confirmed by the general good agreement in bathymetry along individual profiles (Figure 5).

2.1.2. Free-air gravity anomaly (FAA)

The FAA data were derived from global dataset that combined CryoSat-2 and Jason-1 satellite-derived FAA with shipboard measurements (Figure 1(c), V26.1; Sandwell *et al*. 2014, http://topex.ucsd.edu/marine_grav/mar_grav.html) in 1-minute grid. Neumann *et al*. (1993) and Marks (1996) have shown that the satellite-derived free-air anomalies are consistent with shipboard measurements for wavelengths longer than 25–30 km.

2.1.3. Sediment thickness

The sediment thickness data (Figure 1(d)) were extracted from the 5-minute global database of Divins (2003) and supplemented by the data of Yang. *et al*. (2015), and were used to correct for gravitational and loading effects of sediments. The sediment thickness data used are in general agreement with local surveys, although differences in details do exist (Figure 5(a)), which may introduce some uncertainties in the calculated gravity anomalies.

2.1.4. Crustal age

The crustal age data in a 6-minute grid (Figure 1(e)) were extracted from the global datasets of Müller *et al*. (2008) and complemented by more detailed studies (e.g. Li *et al*. 2015). The Müller *et al*. (2008) dataset has already compiled and merged the best available magnetic anomalies. For much of this study, we analysed anomalies along individual magnetic isochrons (e.g. Briais *et al*. 1993; Li *et al*. 2015; Figure 1.)

2.2 Thermal corrections

The gravitational effects of lithospheric cooling, i.e. the thermal corrections (Figure 2), were calculated from a 3D thermal model. The 3D thermal model extends vertically from 0 to 100 km depth, assuming vertical heat transfer (Turcotte and Schubert 2002) in a plate with age given by Müller *et al*. (2008). Temperatures were set to be $T_s = 0$ °C at the surface and T_p = 1350°C at 100 km depth. This thermal structure was then converted into a 3D density grid, $\Delta\rho = \rho_0\alpha(T_0 - T)$, where T_0 and ρ_0 are the reference temperature and density, respectively, and α is the thermal expansion coefficient. T_0 = 1350°C, $\alpha = 3 \times 10^{-5}$°C^{-1}, and $\rho_0 = 3.3 \times 10^3$ kg/m^3 were used in the calculation.

As lithospheric age increases, the temperature versus depth profile change according to the 1D plate cooling model (Turcotte and Schubert 2002). However, when the lithosphere is old enough (e.g. with an age greater than ~100 Ma), the temperature-depth profiles differ little. While this study analysed only the crustal structure of the SCS ocean basins, we need to incorporate the boundary gravitational effects of the surrounding continental lithosphere in order to minimize the edge effects in the gravity modelling. Thus, we experimented with a series of thermal models (Figure 2), for the assumed age of 50–120 Ma for the surrounding continental lithospheric plates with increment of 10 Ma. Different models of RMBA and crustal thickness variations were calculated, to test the sensitivity of modelling results to the assumed age of the surrounding continental area. Analysis showed that the model results of the SCS ocean basin were not highly sensitive to the uncertainties in the assumed mantle temperature structure beneath the continental margins

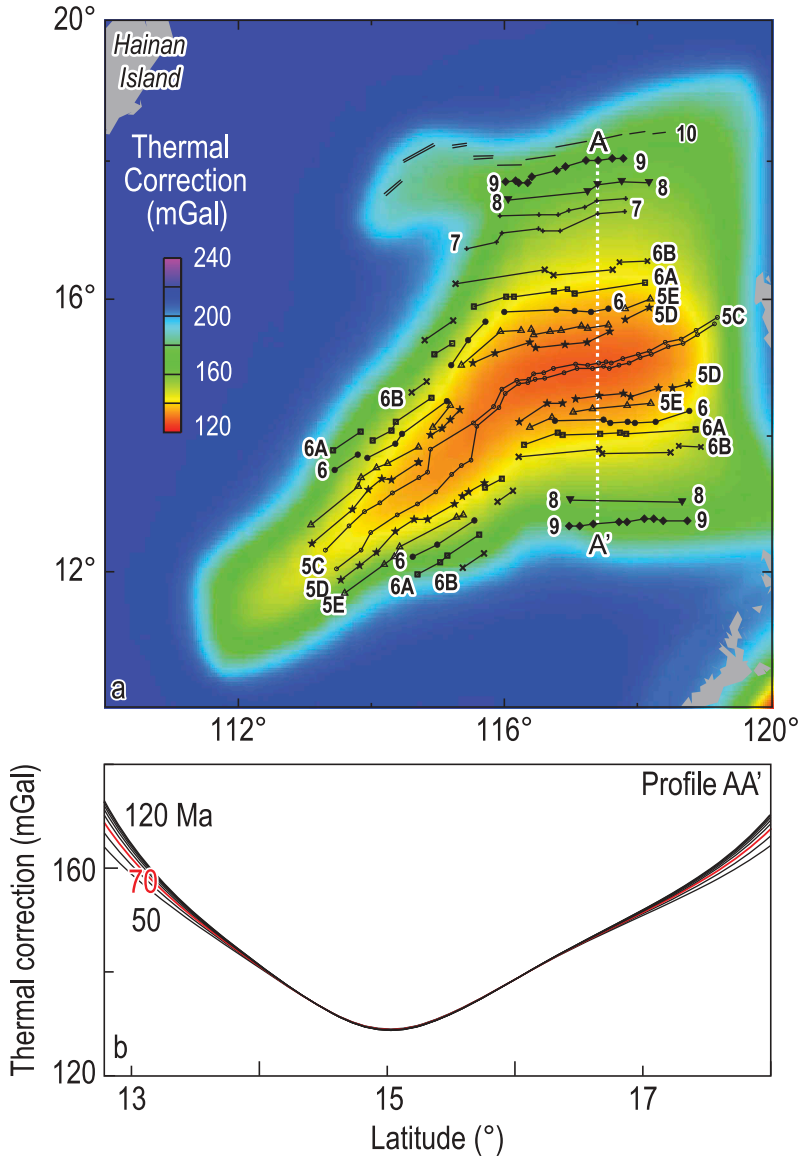

Figure 2. (a) Map of calculated gravity effects of lithospheric cooling, i.e. thermal correction. Crustal age from Müller *et al.* (2008) was used for oceanic crust. To minimize edge effect in modelling the gravity of the oceanic crust, a constant lithospheric age (70 Ma in the case of this map) was assumed for the non-oceanic regions of the study area. (b) Cross-section profile along AA′ on the top panel. Numbers refer to different model lithospheric ages (50–120 Ma) that were assumed for the non-oceanic regions in the thermal models. The 70 Ma model for non-oceanic regions is our best-fitting model based on comparison with the seismic profiles across both the oceanic and non-oceanic regions.

(Figure 2(b)) and there are reasonable fits between our model results and seismic data.

2.3 Residual gravity anomalies and crustal thickness

Mantle Bouguer anomaly (MBA, Figure 1(f)) was calculated following the method of Parker (1973) by subtracting from the free-air anomaly the predicted gravity effects of the water-sediment, sediment-crust, and crust-mantle interfaces for reference crustal thickness of 5.5 km. Densities of water, crust, and mantle were assumed to be 1.03, 2.7, and 3.3 × 10^3 kg/m^3, respectively (Table 1). The sediment layer was divided into 6 sub-layers (Wang *et al.*), and each sub-layer was assigned an average density that increased with depth (Cowie and Karner 1990).

Residual mantle Bouguer anomaly (RMBA) (Figure 3(a)) was then calculated by removing the thermal correction (Figure 2) from the MBA. Previous studies have shown that both crust and mantle density variations contribute to the RMBA (Magde and Detrick 1995; Canales *et al.* 2002). In this study an end-member crustal thickness

Table 1. Model parameters.

Parameter	Description	Value	Unit
ρ_m	Mantle density	3300	kg/m^3
ρ_c	Crust density	2700	kg/m^3
ρ_w	Water density	1030	kg/m^3
η_0	Reference viscosity	10^{19}	Pa s
η_{max}	Maximum viscosity	10^{23}	Pa s
C_p	Specific heat capacity	1250	J/Kg K
k	Thermal conductivity	3	W/m K
Q	Activation energy	$2.5*10^5$	J/mol
R	Universal gas constant	8.3114	J/mol K
T_s	Temperature at the surface of the model mantle domain	0	°C
T_p	Mantle potential temperature	1300–1400	°C
U	Half-spreading rate	0.5–4	cm/yr
U_r	Ridge migration rate	2	cm/yr
g	Gravitational acceleration	9.8	m/s^2
L_{jump}	Length scale of southward ridge jump	20	km

model (Figure 3(b)) was calculated by downward continuation of all the RMBA signals to a constant depth with a crust/mantle density contrast of 0.6×10^3 kg/m^3 (Kuo and Forsyth 1988; Lin *et al.* 1990; Wang *et al*).

2.4 Residual bathymetry

Residual bathymetry anomaly (RBA) (Figure 3(c)) was defined as the observed seafloor bathymetry after subtracting the predicted sediment loading and thermal subsidence due to plate cooling. The predicted thermal subsidence due to plate cooling was calculated using the same 1D mantle thermal model (Turcotte and Schubert 2002) as used for the RMBA calculation. The sediment loading correction was calculated assuming Airy compensation: $\Delta Z = h_s\,(\rho_m - \rho_s)/(\rho_m - \rho_w)$, where ΔZ is the correction to bathymetry, h_s is sediment thickness. ρ_m, ρ_s and ρ_w are densities of the mantle, sediment, and water, respectively, which are the same as used in the gravity calculations.

3. Results

3.1 Comparison with seismic profiles

To evaluate the robustness of the gravity modelling results, we compared our gravity-derived crustal thickness models to the crustal thickness values determined by the seismic studies in the SCS ocean basin (Figures 4–6). We compared 14 seismic profiles (Yan *et al.* 2001; Zhou *et al.* 2005; Zhao *et al.* 2010; Lv *et al.* 2011; Qiu *et al.* 2011; Ruan *et al.* 2011, 2016; Wei *et al.* 2011; Wu *et al.* 2011; Ao *et al.* 2012; He *et al.* 2016; Zhang *et al.* 2016) of the bathymetry, sediment thickness, and gravity-derived Moho depth to the seismic measurements, focusing especially on profiles that transect the SCS oceanic crust (Figure 4). The gravity and seismic results agree relatively well in the overall trends of variations (see selected examples in Figure 5), especially in oceanic crust (Figure 6). There might be a few causes of the local differences between the gravity and seismic models: (1) The sediment thickness data used in our gravity modelling might lack the resolution in some localities; (2) There might be lateral density variations along seismic profiles, which were not considered in the gravity modelling (e.g. Zhao *et al.* 2010; Ruan *et al.* 2016); (3) Several seismic profiles strike across the continental margin area, where the gravity edge effects from the assumed continental lithospheric ages might cause uncertainties. Although the gravity-derived crustal thickness model would inevitably differ from that of the seismically determined crustal structure due to the fundamental differences in data types and methodologies, both the gravity and seismic data provide important constraints on the spatial variations of crustal and mantle properties of the SCS.

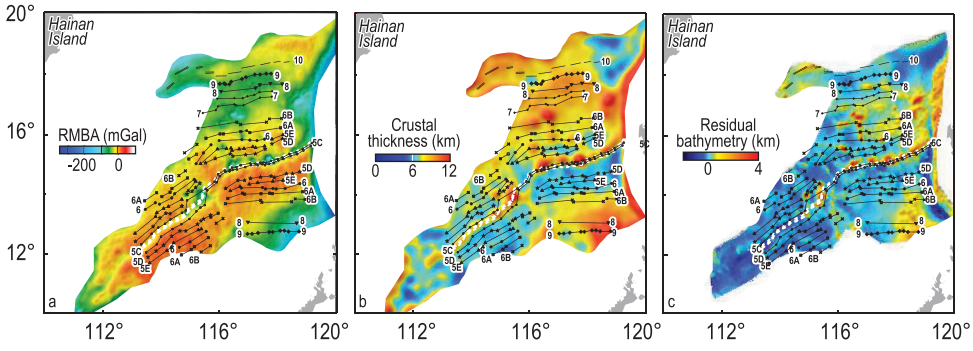

Figure 3. (a) Calculated residual mantle Bouguer anomaly (RMBA) by removing the gravity effect of lithosphere cooling from MBA. (b) Map of crustal thickness variations derived from RMBA assuming that all RMBA variations are caused by crustal thickness variations. An average crustal density of 2.7×10^3 kg/m^3 and mantle density of 3.3×10^3 kg/m^3 were assumed. (c) Residual bathymetry anomaly (RBA), calculated from subtracting the predicted thermal subsidence and sediment loading from the observed seafloor bathymetry.

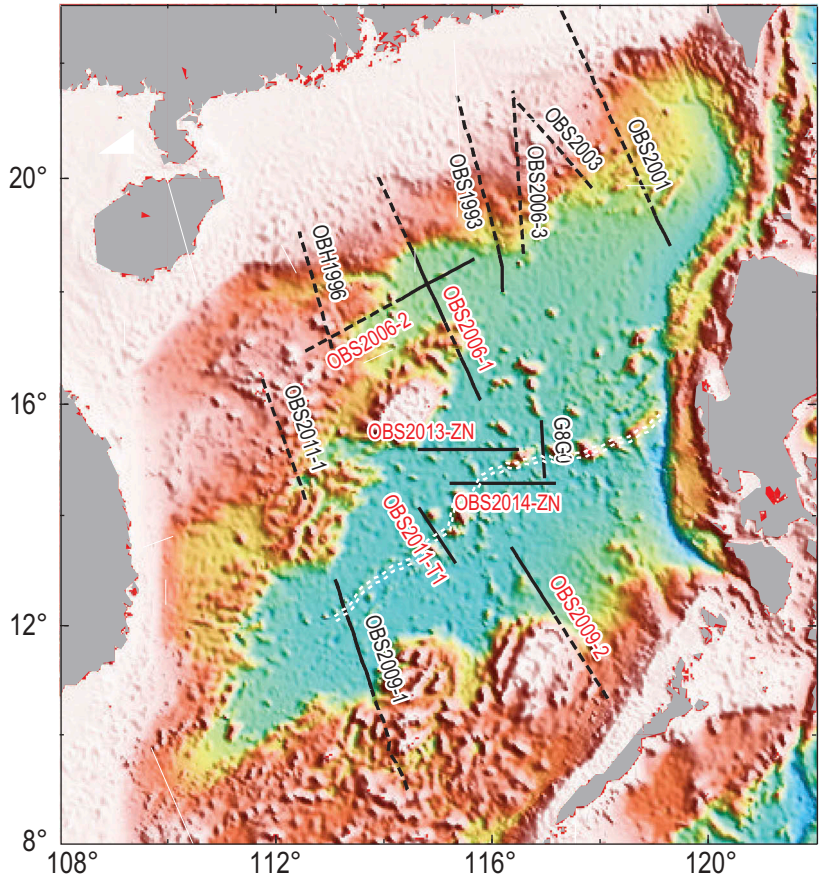

Figure 4. A selection of seismic profiles in the SCS. Profiles over the oceanic crust are shown by solid lines, while those over continental margins by dotted lines. Red solid lines show selected seismic profiles over oceanic crust as illustrated in Figure 5. Data for seismic profiles were from Yan *et al.* (2001) (OBS1993); Zhou *et al.* (2005) (OBS2003); Zhao *et al.* (2010) (OBS2001); Lv *et al.* (2011) (OBS2011-1); Qiu *et al.* (2011) (OBS2009-1); Ruan *et al.* (2011) (OBS2009-2); Wei *et al.* (2011) (OBS2006-3); Wu *et al.* (2011) (OBS2006-1); Ao *et al.* (2012) (OBS2006-2); Qiu *et al.* (2001) (OBH1996); Ruan *et al.* (2016) (OBS2013-ZN, OBS2014-ZN); He *et al.* (2016) (G8G0); Zhang *et al.* (2016) (OBS2011-T1).

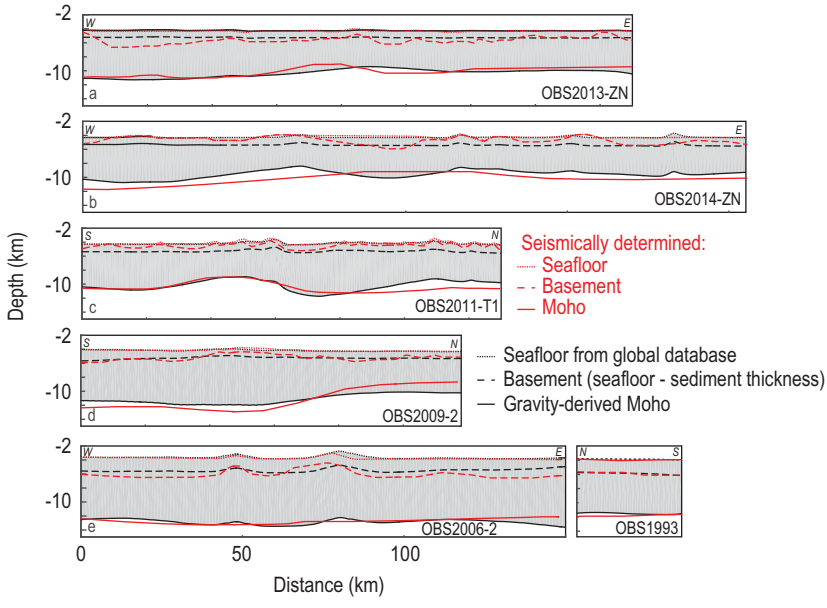

Figure 5. Selected examples (red lines in Figure 4) of depth sections in oceanic crust, showing the topography, basement, and Moho in the gravity-derived models (black lines) versus the corresponding values determined seismically (red lines). Depths shown are relative to the sea level.

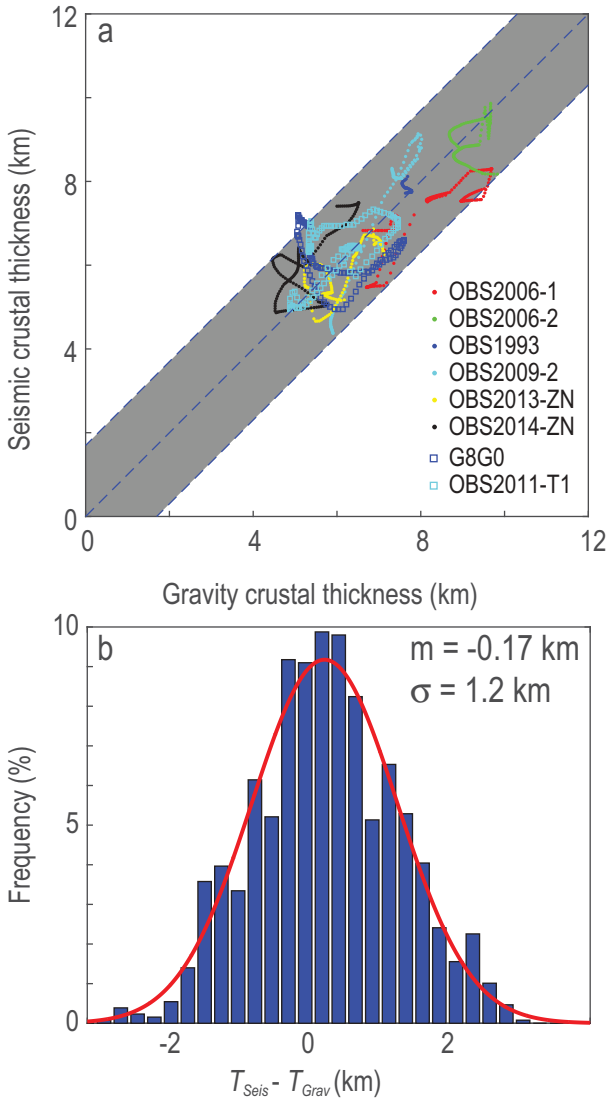

Figure 6. Comparison of the gravity-derived crustal thickness with seismic profiles for oceanic crust. (a) Values of the gravity-derived versus seismically determined crustal thickness values along individual profiles. Shaded area represents the value differences between the gravity-derived and seismically determined crustal thickness of less than 1 km. (b) Frequency distribution of the difference between the gravity-derived and seismically determined crustal thickness values.

3.2 Regional variations in gravity and topographic anomalies

In the SCS East Sub-basin, the extinct spreading axis between 116°-119°E can be easily tracked as isolated patches of negative RMBA (Figure 3(a)) and relatively thick crust (Figure 3(b)). These patches of relatively thick crust can range up to 50–100 km in spatial dimension (Figure 3(a,b)). Correspondingly, the extinct spreading centre is associated with local residual topographic highs of up to 2–4 km (Figure 3(c)). Negative RMBA and positive RBA with similar amplitude and dimensions were also observed near 115°E at the eastern end of the extinct spreading axis in the Southwest Sub-basin.

Our results showed prominent north-south asymmetry in the distribution of RMBA (Figure 3(a)), crustal thickness (Figure 3(b)), and RBA (Figure 3(c)). In general, the northern flank of the SCS ocean basin is associated with more negative RMBA, more prominent RBA and thicker crust (Figure 7). Between chron C8n (~25.18 Ma) and C5Dn (~17.38 Ma), the isochon-averaged north-south differences in RMBA are about 20–40 mGal (Figure 7(m)), crustal thickness differences are about 0.5–1 km (Figure 7(o)), and RBA differences are about 0.1–0.5 km (Figure 7(n)), respectively. For chron C9n (~26.93 Ma), isochron-averaged values of the southern SCS exhibit negative RMBA, positive RBA, and thicker crust. We suspect that chron C9n might be too close to the southern continent-ocean boundary (COB), and thus the result for the chron C9n in the southern flank might be relatively unreliable due to the gravitational edge effects. The calculated differences between the N-S isochron conjugates are found to be greater than the standard deviations of the along-isochron variations (Figure 7(m–o)), indicating that the observed N-S asymmetry in RMBA is relatively robust.

4. Discussion: geodynamic interpretations of the observed asymmetry

We investigated the potential causes of the asymmetry in the calculated crustal thickness through 2D numerical modelling of the following five tectonic and mantle scenarios: (1) asymmetric and variable spreading rates, (2) ridge jump, (3) ridge migration, (4) asymmetric mantle temperatures, and (5) asymmetric mantle depletion (Figure 8). We used the finite-element software package COMSOL Multiphysics 5.0 to calculate the plate-driven flow of incompressible mantle and the associated thermal structure, assuming a temperature-dependent viscosity. The equations for conservation of mass, momentum, and energy are given by

$$\frac{\partial \rho_m}{\partial t} + \rho_m \nabla \boldsymbol{u} = 0 \tag{1}$$

$$-\rho_m \frac{\partial}{\partial_t} \boldsymbol{u} - \nabla p + \eta_{eff} \nabla^2 \boldsymbol{u} = 0 \tag{2}$$

$$\rho_m C_p \frac{\partial T}{\partial_t} + \rho_m C_p \boldsymbol{u} \nabla T - k \nabla^2 T = 0 \tag{3}$$

respectively, where ρ_m is mantle density, $\boldsymbol{u}$ is velocity vector, p is pressure, η_{eff} is effective mantle viscosity, C_p is specific heat, T is temperature, k is

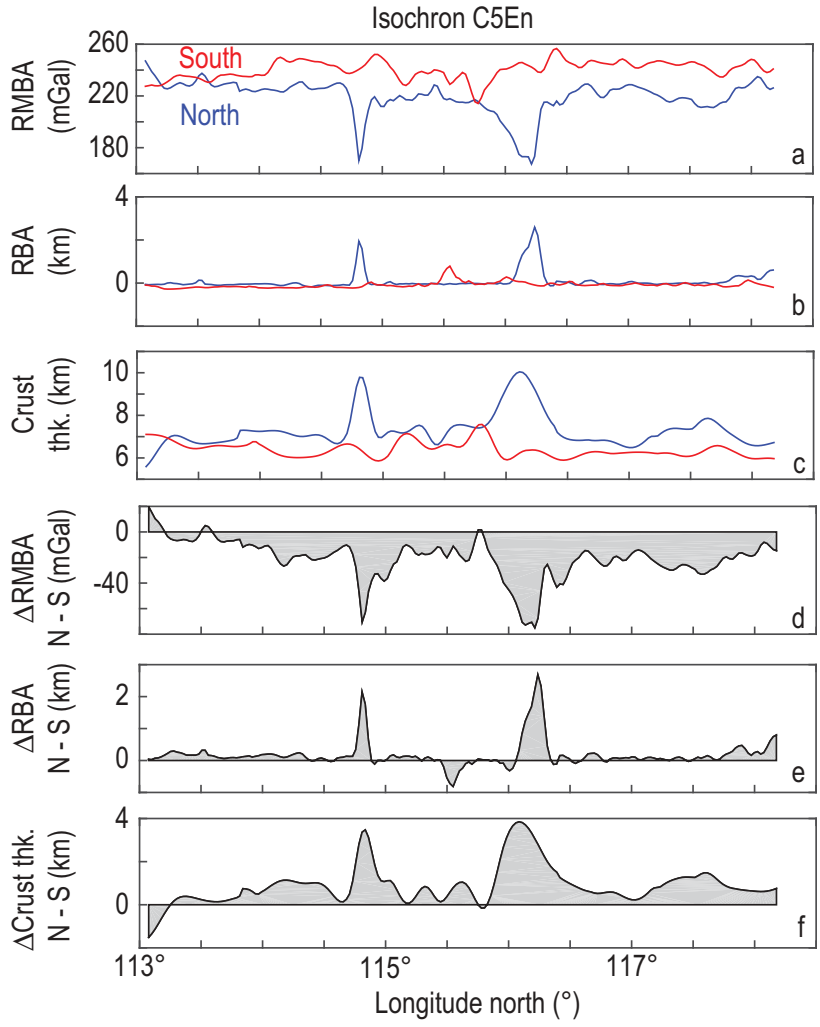

Figure 7. (a-f) Selected example of along-isochron profiles (for chron C5En) of RMBA, crustal thickness, and RBA along the N-S conjugates within the ocean basin. The southern profiles (red lines) were rotated to the north (blue lines) and plotted along the northern flank longitude. The differences in RMBA and RBA were defined as the along-isochron values of the northern flank subtracted by the conjugate points on the southern flank. (g-l) Same as in panels (a-f) but for chron 6CAn. (m-o) Along-isochron averaged values of the N-S differences in RMBA, crustal thickness, and RBA versus crustal age using the time scale of Gradstein *et al.* (2012). Between 26 and 17 Ma, the northern flank of the SCS ocean basin is associated with more negative RMBA and more prominent RBA, indicating thicker crust or less dense mantle compared to the southern conjugate.

thermal conductivity, and $\frac{\partial}{\partial_t}$ is time derivative. If the model flow is steady state, the time derivative term vanishes.

The temperature-dependent viscosity is calculated by

$$\eta_{td} = \eta_0 \exp\left[\frac{Q}{R}\left(\frac{1}{T} - \frac{1}{T_p}\right)\right] \quad (4)$$

where η_0 is the reference viscosity (10^{19} Pa·s), Q is activation energy, and R is the universal gas constant. The effective mantle viscosity is defined by

$$\eta_{eff} = \left(\frac{1}{\eta_{td}} + \frac{1}{\eta_{\max}}\right)^{-1} \quad (5)$$

where η_{max} is the maximum viscosity (10^{23} Pa·s, e.g. Gregg *et al.* 2009).

In the simulations, mantle flow was driven by imposing horizontal velocities perpendicular to the mid-ocean ridge along the top boundary of the model space. The spreading rates of the two ridge flanks were assumed to be asymmetric and variable for the first case (Figure 8(a)) but symmetric and constant for the rest of cases (Figure 8(b–e)). The base of the model was set to be stress free (Figure 8(a,b,d and e)), allowing for convective flux without resistance from the underlying mantle. In the ridge migration model (Figure 8(c)), the base of the model was set to move with the ridge migration rate U_r of 2 cm/yr. The sides of the model were also stress free. The temperatures at the top and

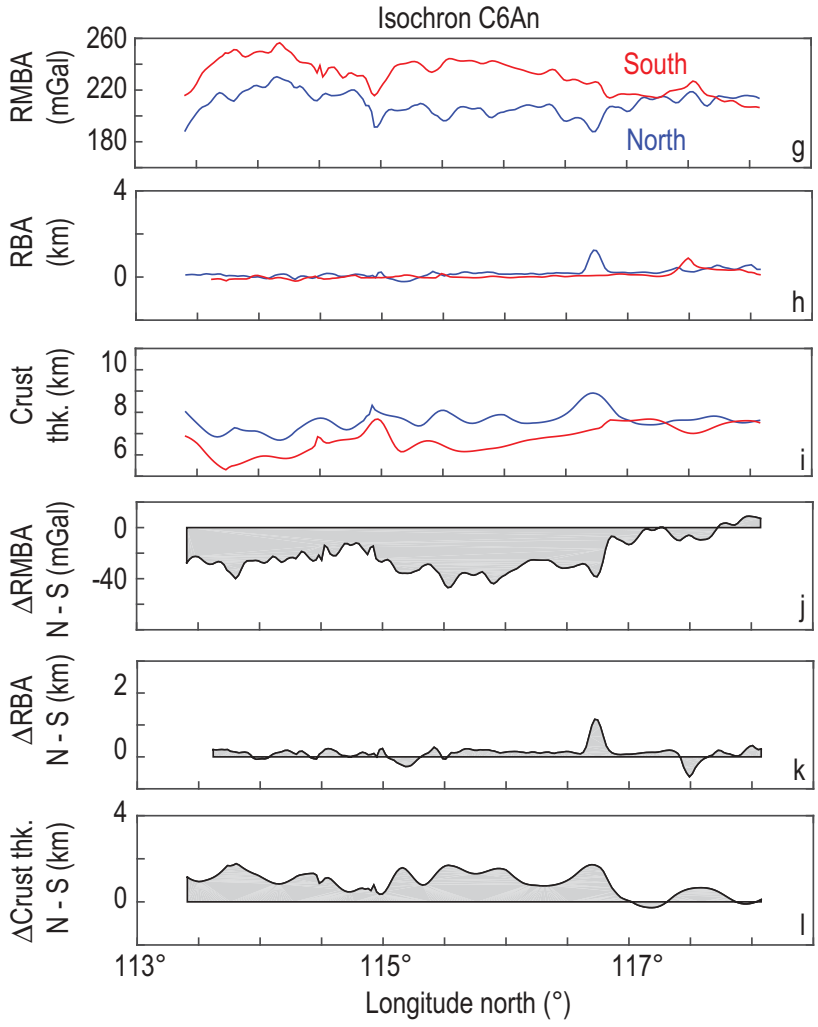

Figure 7. (Continued).

the base of the model space were set to T_s = 0°C and T_p = 1,300–1400°C, respectively. The heat flux across the left and right sides of the model was assumed to be zero. Model parameters were given in the Table 1.

Based on the above modelled thermal structure, we calculated the extent of melting at all points in the model domain using the BG15 anhydrous melting model (Behn and Grove 2015). Constant melt productivity of 1% kbar^{-1} and an adiabatic gradient of 1.5°C kbar^{-1} were assumed in the melting model. The mantle compositions input into the BG15 model were assumed to be the DMM compositions of Workman and Hart (2005) or the depleted DMM compositions (Behn and Grove 2015). At each melting step, 90% of the generated melt was removed and accumulated elsewhere, while allowing the remaining melts and depleted mantle to ascend and be further melted at the next melting step. The melt production rate was defined as the product of the melt productivity and the mantle upwelling velocity U_z. The upwelling velocity was determined from the mantle flow models.

We assumed that once melts are generated in the mantle, the melt patches would migrate vertically to the bottom of an impermeable 'lithospheric lid' and then flow upslope along the base of the lid towards the ridge axis (Sparks and Parmentier 1991; Sparks *et al.* 1993; Magde and Sparks 1997; Magde *et al.* 1997). However, instead of assuming all melts would first mix at the ridge axis and then partition equally to the two ridge flanks, we alternatively assumed that most melts would pool only at the side of the ridge flank where the melts were generated, and thus contribute only to crustal thickness of that ridge flank. For each flank, the crustal thickness was calculated by integrating the melts production rate over the melting region and dividing by the spreading rate (Forsyth 1993).

4.1 Asymmetric and variable spreading rates

The half-spreading rate of the SCS varied in the range of 1–4 cm/yr in the East Sub-basin (Li and Song 2012; Song and Li 2012; Li *et al.* 2014). We first calculated

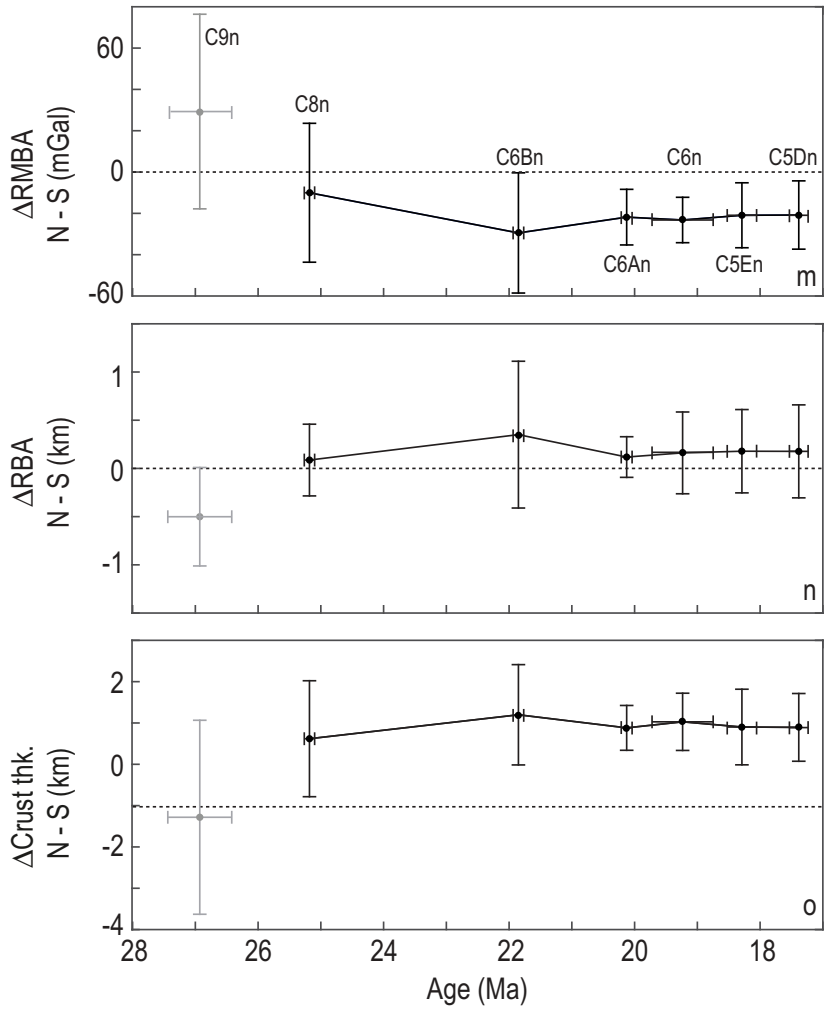

Figure 7. (Continued).

models of constant half-spreading rates based on the melting scheme of Behn and Grove (2015; Figure 8(a)). The models predict relative strong increase in crustal thickness with spreading rate for half-spreading rate less than 2 cm/yr, but only relatively small increase for half-spreading rate greater than 2 cm/yr (Figure 14(a)). The models also predict that the mantle temperature has major influence on the calculated crustal thickness (Figure 14(a)).

While there are significant discrepancies in the calculated SCS spreading rates between various studies (e.g. Li and Song 2012; Song and Li 2012; Li *et al*. 2014), analysis of the relatively high-resolution deep-tow magnetic data revealed that relative to the southern conjugate, the northern flank was associated with faster spreading rates during ~33–25 Ma, slower rates during ~25–22 Ma, and similar rates at ~22–15 Ma (Li *et al*. 2014). Geodynamic calculations based on the Li *et al*. (2014) spreading rate models Figures 9, 14(b), S1(a), and S2 predicted up to 0.4 km thicker crust at the northern flank at ~29 Ma, but ~0.2 km thinner crust at the northern flank at ~25 Ma. Thus the models of asymmetric and variable spreading rates would produce alternating thicker and thinner crust on the northern flank, which cannot explain the observed systematically thicker crust on the northern flank (Figure 7(m–o)). For the remaining four models of ridge jump, ridge migration, asymmetric mantle temperature, and asymmetric mantle composition sources, respectively, we assumed a constant average half-spreading rate of 2 cm/yr based on the spreading rate models of Li *et al*. (2014) .

4.2 Southward ridge jump

A southward ridge jump of ~20 km occurred around 23.6 Ma in the East Sub-basin (Xu *et al*. 2011; Li *et al*. 2014, 2015). We used a time-dependent numerical model to study the effects of ridge jump on melt production and resultant crustal structure (Figure 10). Steady-state mantle flow and thermal structure were assumed before ridge jump (33–23.6 Ma, Figure 10(a, b). We first calculated mantle flow and temperature fields for a steady-state

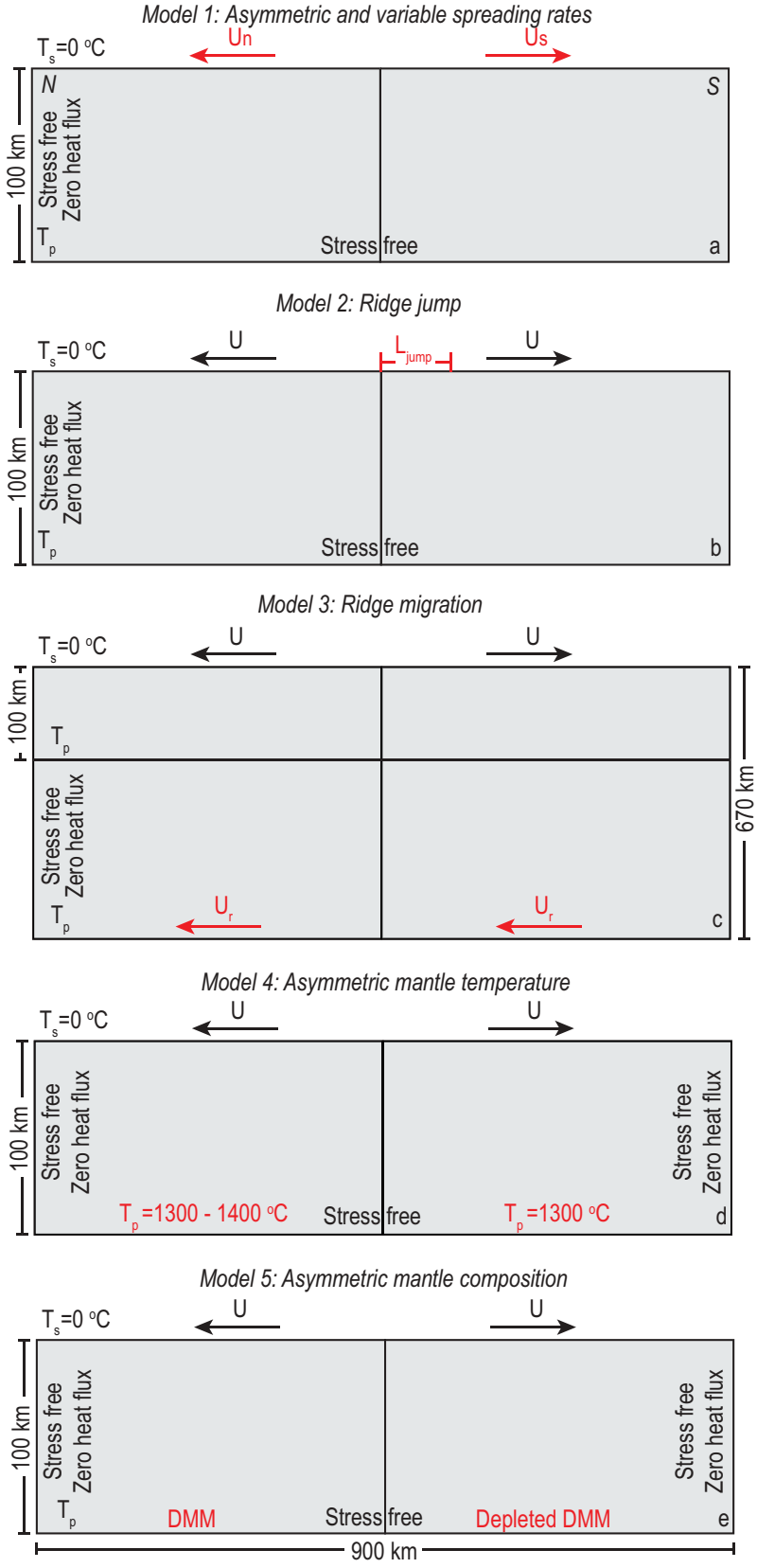

Figure 8. Schematic diagrams illustrating the model domain and boundary conditions for 2D thermal models: (a) Asymmetric and variable spreading rates; (b) Southward ridge jump; (c) southward ridge migration; (d) asymmetric mantle temperature; and (e) asymmetric mantle composition due to different degree of mantle depletion. Model parameters include half-spreading rate, U; temperature at the surface, T_s, and at the base of the model domain, T_p; the length scale of ridge jump, L_{jump}; ridge-normal migration rate, U_r, and the mantle composition model DMM of Workman and Hart (2005).

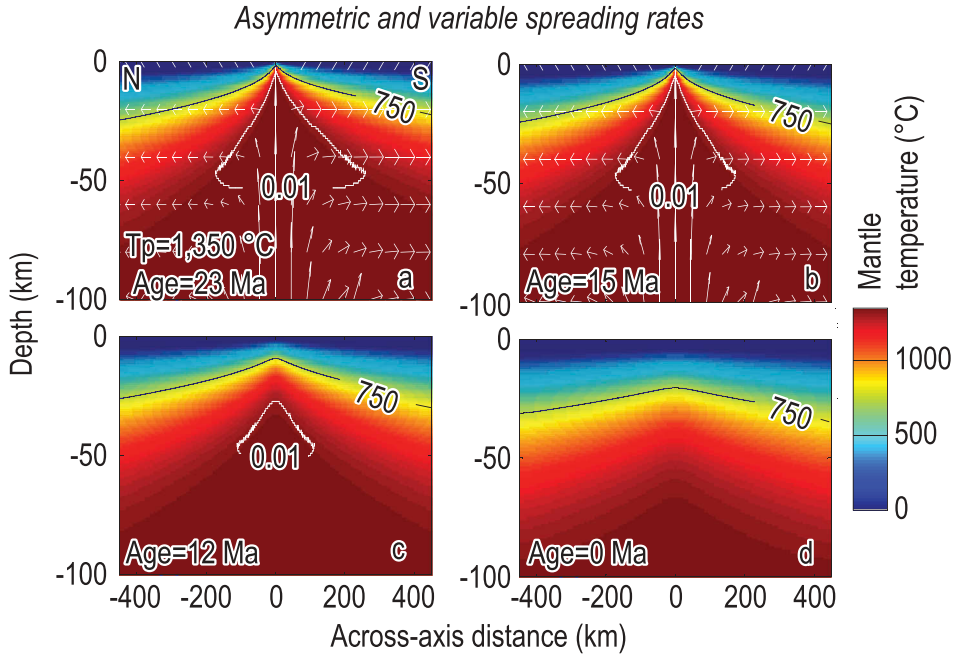

Figure 9. Comparison of the predicted crustal thickness of the northern and southern flanks for the models of asymmetric and variable spreading rates. Relative to the southern conjugate, the half-spreading rate of the northern flank is calculated to be faster at ~33–25 Ma, slower at ~25–22 Ma, and similar at ~22–15 Ma, based on the deep-tow magnetic model of Li *et al*. (2014); (a) Half-spreading rate of the northern flank was slower relative to the southern flank at 23 Ma. (b) Half-spreading rate was the same on the northern and southern flanks at 15 Ma; (c and d) After cessation of seafloor spreading, the N-S differences become even smaller. All models have T_p = 1350°C.

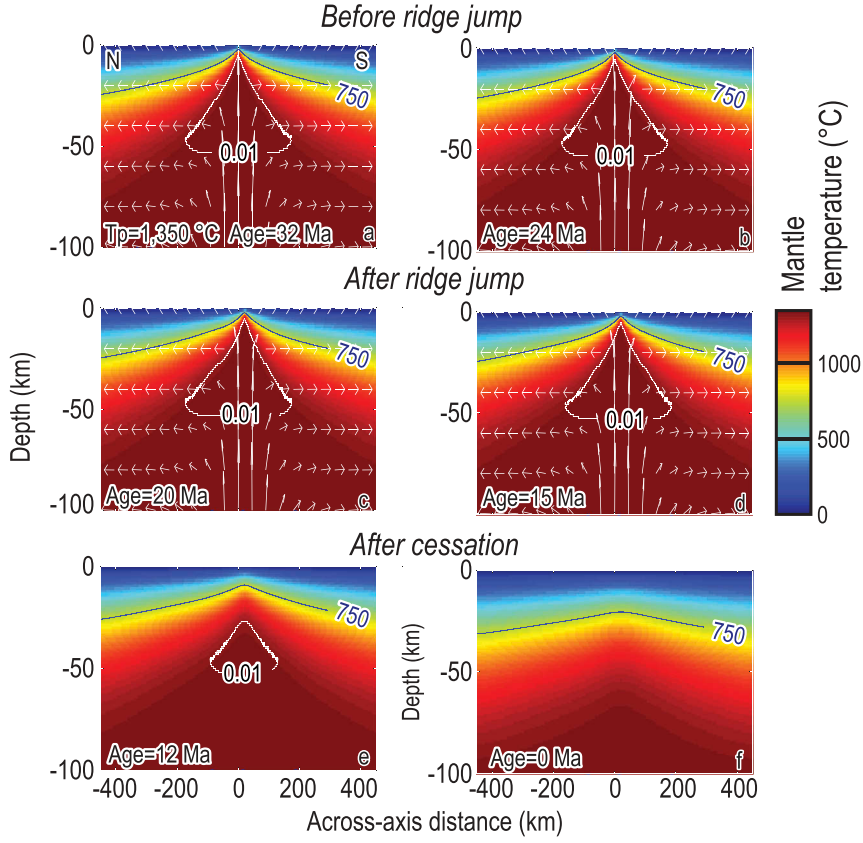

Figure 10. Comparison of the predicted crustal thickness of the northern and southern flanks for the models of southward ridge jump. (a and b) Before ridge jump; (c and d) After ridge jump; (e and f) After cessation of seafloor spreading.

model with a half-spreading rate of 2 cm/yr. We then moved the spreading centre southward by 20 km, and set up a time-dependent model using the steady-state results as initial values. The time-dependent calculations were conducted for every 0.5 Ma for a total time period of 9 Ma (23.6–14.6 Ma).

The southward ridge jump was calculated to cause higher mantle temperature in the northern flank than the southern conjugate (Figure 10(c)), generating thicker crust in the northern flank (Figure 14(c)). Results of calculations showed several features: (1) The N-S difference in the predicted crustal thickness reached its maximum value (~2 km) when the ridge jump just occurred. However, the N-S asymmetry in crustal thickness is calculated to be limited only to crustal ages of 23.6–20 Ma Figures 14(c), S1(b), and S3. Thus, the southward ridge jump alone cannot explain the observed N-S asymmetry for a wide crustal age span from chron C8n (~25.18 Ma) to C5Dn (~17.38 Ma) (Figure 7(m–o)) (2) The N-S difference in the crustal thickness was calculated to increase with increasing mantle temperature due to the ridge jump (Figure 14(d)). (3) About 6 Ma after the ridge jump, there was little difference in the predicted crustal thickness between the northern and southern flanks (Figure 14(c, d)).

4.3 Southward ridge migration

In the East and Southwest Sub-basins, the southward ridge migration rate was estimated to be 2.4 cm/yr and 1.4 cm/yr, respectively (Li *et al*. 2015). We set up a steady-state model with a ridge migration rate U_r of 2 cm/yr to investigate the effects of ridge migration on mantle flow and thermal structure. The full thicknesses of the lithospheric and asthenospheric layers were assumed to be 100 and 670 km, respectively (Figure 8(c)). A horizontal velocity of 2 cm/yr to the north was applied at the base of the model, while we solved for the mantle flow field in the ridge-fixed reference frame.

The southward ridge migration was calculated to result in greater vertical velocity on the leading (south) side of the ridge than that on the trailing (north) side, generating more melts on the leading side (Figures S1(c) and S4). As a result, the crust of the northern flank was calculated to be thinner than that of the southern flank (Figures 11 and 14(e)). Thus the southward ridge migration cannot explain the observed more negative RMBA and thus the inferred thicker crust on the northern flank (Figure 7(m–o)). Furthermore, the calculated N-S difference is small (less than 0.2 km). The N-S difference in crustal thickness was calculated to increase with increasing mantle temperature (Figure 14(f)).

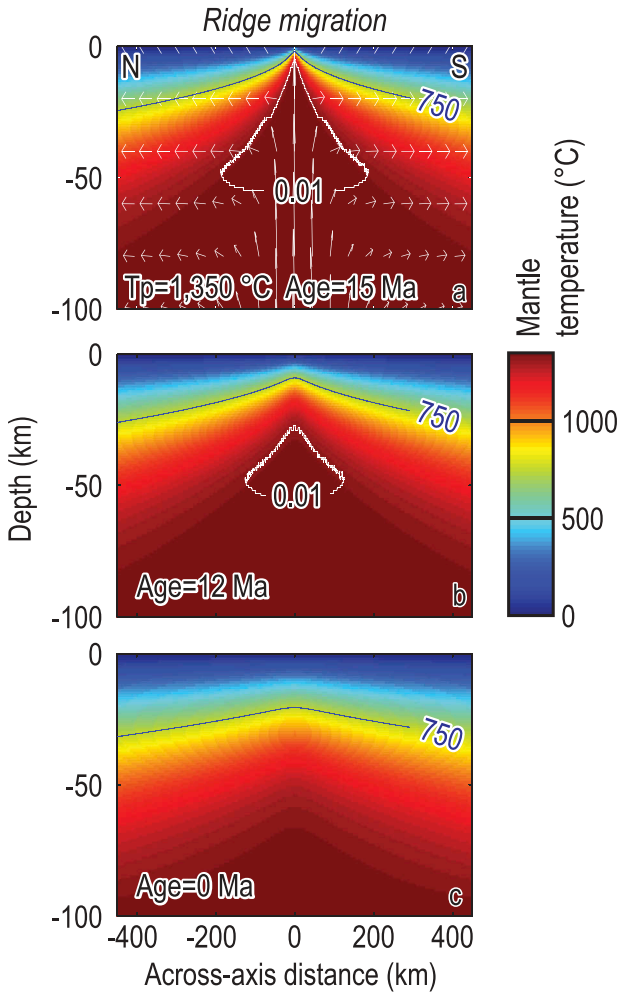

Figure 11. Comparison of the predicted crustal thickness of the northern and southern flanks for the models of southward ridge migration. (a) Age = 15 Ma; (b) Age = 12 Ma; (c) Age = 0 Ma. All models have T_p = 1350°C.

4.4 Asymmetric mantle temperature

To examine the effects of asymmetric mantle temperature, we fixed the mantle temperature of the southern flank at T_{p_south} = 1300°C, while changed the mantle temperature of the northern flank T_{p_north} to be 1300–1400°C with step increments of 25°C (Figures 8(d) and 12). The calculated N-S difference in the crustal thickness (Figure 14(g)) increases with the difference in mantle temperature Figures 14(h), S1(d), and S5. A rise of 25°C in mantle temperature could cause an increase of about 1 km in the N-S difference of the crustal thickness (Figure 14(h)). Furthermore, we investigated the changes in the asymmetric thermal structures after the cessation of seafloor spreading, assuming a steady-state half spreading rate of 2 cm/yr, T_{p_north} of 1350°C, and T_{p_south} of 1300°C (Figure 12). The results show that the differences in the

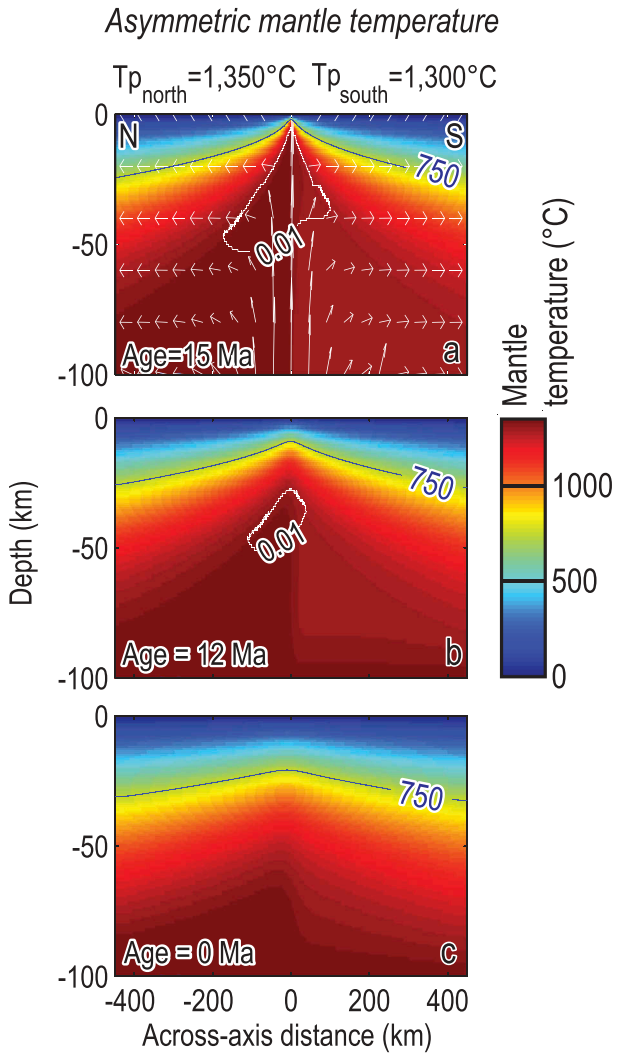

Figure 12. Comparison of the predicted crustal thickness of the northern and southern flanks for the models of asymmetric mantle temperature. All models have T_{p_north} = 1350°C and T_{p_south} = 1300°C. (a) Age = 15 Ma; (b) Age = 12 Ma; (c) Age = 0 Ma.

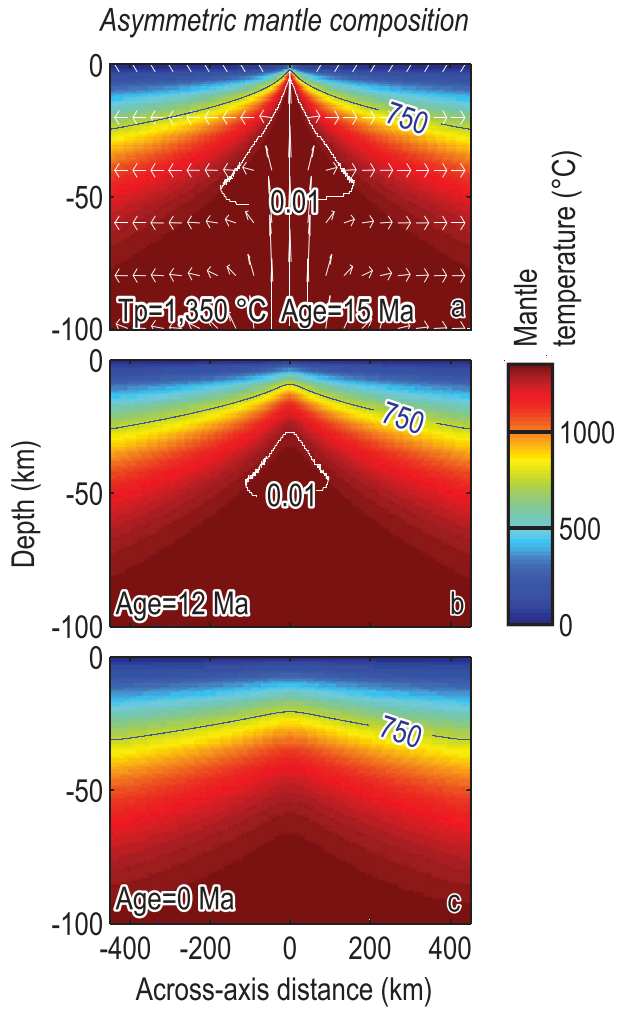

Figure 13. Comparison of the predicted crustal thickness of the northern and southern flanks for the models of asymmetric mantle depletion. All models have T_p = 1350°C and 2% more depleted mantle source under the southern flank. (a) Age = 15 Ma; (b) Age = 12 Ma; (c) Age = 0 Ma.

thermal structure caused by the initial asymmetric mantle temperatures were maintained after the cessation of seafloor spreading in the SCS Figures 12(b,c) and 15.

4.5 Asymmetric mantle compositions

Here, we examined the influence of mantle depletion on crustal thickness. We applied the DMM compositions of Workman and Hart (2005) to the northern flank (Figure 8(e)). For the mantle compositions of the southern flank, we first extracted a small amount of melt (1 or 2% melt) from the DMM compositions of Workman and Hart (2005) using BG15 melting model (Behn and Grove 2015), and then used this depleted mantle source as the initial compositions of the southern flank (Figures 8(e) and 13). The mantle depletion was calculated to result in slightly thinner crust on the southern flank Figures 14(i), S1(e), and S6. For the model of mantle depletion difference of 2% and T_p = 1350°C, the predicted difference in crustal thickness is about 0.5 km, which is of the same order of magnitude as the observed N-S asymmetry (Figure 7(m–o)). The predicted difference in crustal thickness also increases with increasing mantle temperature Figures 14(j) and 15.

5. Conclusions

(1) Systematic north-south asymmetry was observed in RMBA, gravity-derived crustal thickness, and RBA, indicating possible asymmetry in melt input between the two ridge flanks. For crustal

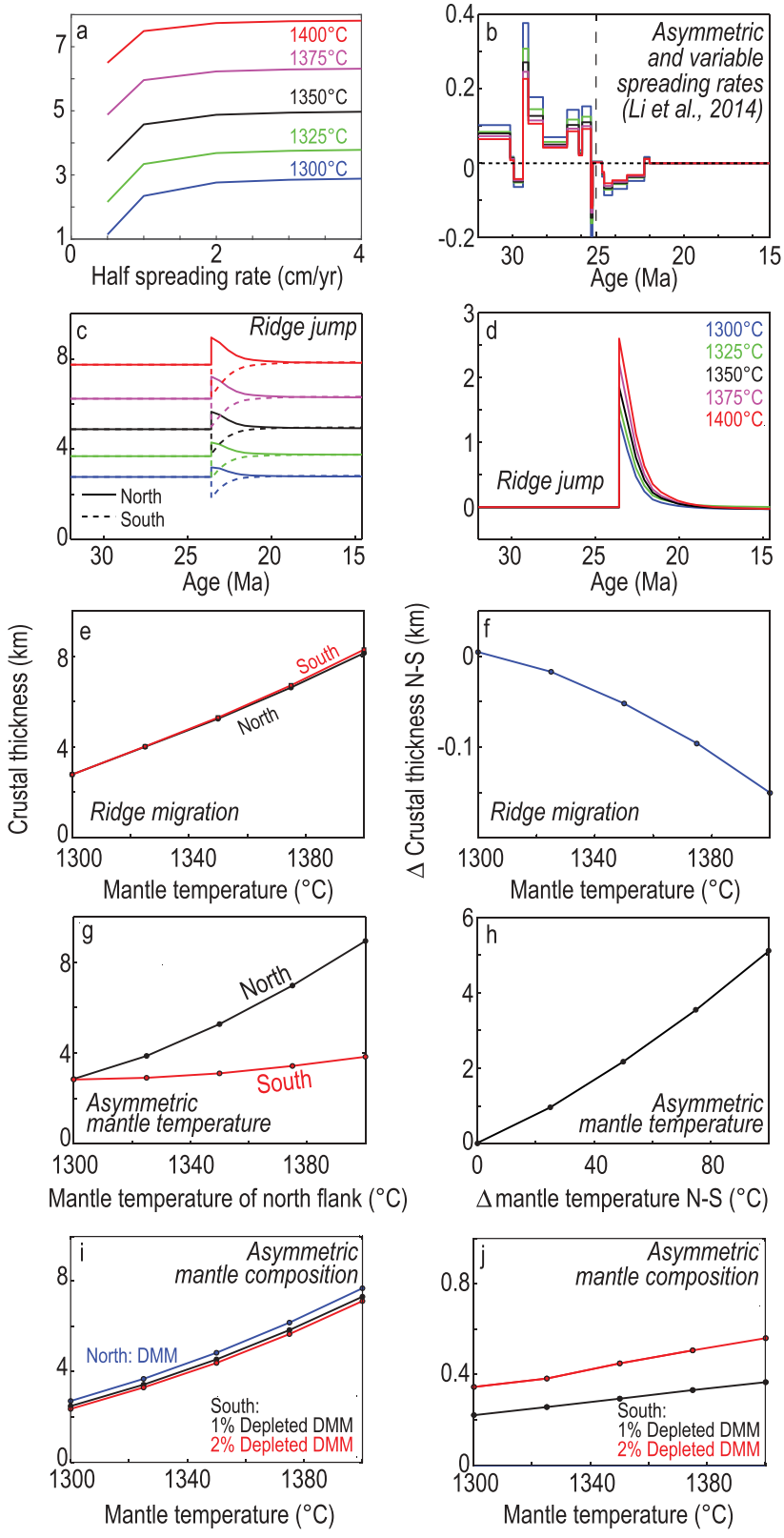

Figure 14. (a) The calculated crustal thickness as a function of seafloor spreading rate and mantle temperature. (b) The calculated N-S differences in crustal thickness based on the asymmetric and variable spreading rate model of Li *et al.* (2014). (c and d) The calculated crustal thickness models of the southward ridge jump as a function of the time after the jump, showing the predicted crustal thickness (c) and the N-S difference in crustal thickness (d). (e and f) The calculated crustal thickness models of the southward ridge migration as a function of mantle temperature, showing the crustal thickness (e) and the N-S difference in crustal thickness (f). (g and h) Same as (e) and (f) except for the models of asymmetric mantle temperature. (i and j) Same as (e) and (f) except for models of asymmetric mantle sources of different degree of depletion.

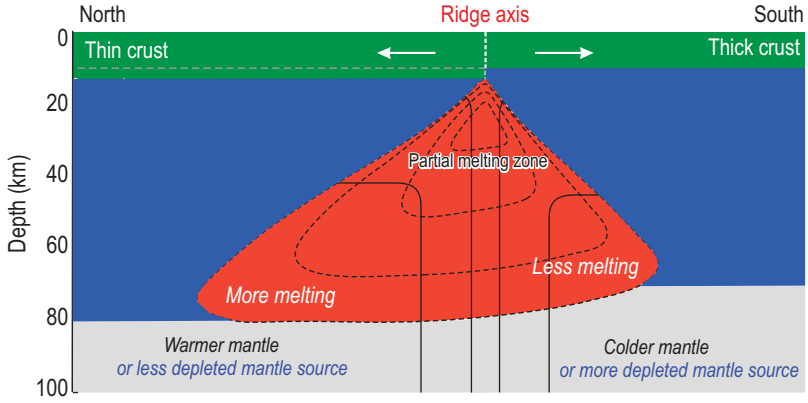

Figure 15. Schematic illustration showing asymmetric spreading model of the upper mantle down to 100 km. Vertical white dashed line shows the ridge axis. Arrows show the mantle flow direction. The pink triangle shows the partial melting zone. The green shade illustrates crustal thickness. Light blue shade marks depleted mantle. The northern flank was assumed to have higher mantle temperature or less depleted mantle source than the southern flank, resulting in thicker crust.

age between chron C8n (~25.18 Ma) and C5Dn (~17.38 Ma), the northern flank of the SCS ocean basin is associated with systematically more negative RMBA and slightly more prominent RBA, indicating thicker crust and/or lighter mantle beneath the northern SCS than the southern conjugate. The calculated N-S differences are greater than the standard deviations of the along-isochron variations, indicating that the observed N-S asymmetries in RMBA and gravity-derived crust are relatively robust.

(2) The extinct spreading axis at the East SCS Subbasin is associated with isolated patches of negative RMBA, thicker gravity-derived crust, and local topographic highs, indicating local excess magmatism along the extinct spreading centre.

(3) Geodynamic models of mantle upwelling and melting revealed that the model of asymmetric and variable spreading rates based on the relatively high-resolution deep-tow magnetic analysis would predict alternating thicker and thinner crust at the northern flank, which is inconsistent with the observed systematically thicker crust on the northern flank. Episodic southward ridge jumps could produce the N-S asymmetry only for crustal age of 23.6–20 Ma. Meanwhile, the southward migration of the SCS ridge axis would predict slightly thinner rather than thicker crust at the northern flank. Thus the above models cannot explain the observed N-S asymmetries in the SCS. On the other hand, higher mantle temperature of up to 25–50°C or >2% less depleted mantle sources on the northern flank could produce large enough anomalies to explain the observed N-S asymmetries.

Acknowledgements

We benefited from discussion with Drs. Hongfeng Yang, Zhiyuan Zhou, Tao Zhang, and the SCSIO Deep Ocean Geodynamics Group. This work was supported by the International Ocean Discovery Program Exp. 349, the National Natural Science Foundation of China [Grant Number 91628301], the NSFC-Shangdong Joint Fund for Marine Science Research Centers [Grant Number U1606401], the Chinese Academy of Sciences [Grant Numbers Y4SL021001, QYZDY-SSW-DQC005], and the National Natural Science Foundation of China [Grant Number 41676027], For data access, please contact Dr. Jian Lin (jlin@whoi.edu).

Disclosure statement

No potential conflict of interest was reported by the authors.

Funding

This work was supported by the National Natural Science Foundation of China; [Grant Number 91628301]; NSFC-Shangdong Joint Fund for Marine Science Research Centers; [Grant Number U1606401]; the Chinese Academy of Sciences; [Grant Numbers Y4SL021001, QYZDY-SSW-DQC005]; National Natural Science Foundation of China; [Grant Number 41676027].

References

Ao, W., Zhao, M., Qiu, X., and Ruan, A., 2012, Crustal structure of the Northwest Sub-basin of the South China Sea and its tectonic implication: Earth Science, v. 37, p. 779–790. [In Chinese.]

Behn, M.D., and Grove, T.L., 2015, Melting systematics in mid-ocean ridge basalts: Application of a plagioclase-spinel melting model to global variations in major element chemistry and crustal thickness: Journal of Geophysical Research, v. 120, p. 4863–4886.

Braitenberg, C., Wienecke, S., and Wang, Y., 2006, Basement structures from satellite-derived gravity field: South China

Sea ridge: Journal of Geophysical Research, v. 111, p. 1–15. doi:10.1029/2005JB003938

Briais, A., Patriat, P., and Tapponnier, P., 1993, Update interpretation of magnetic anomalies and seafloor spreading stages in the South China Sea: Implications for the tertiary tectonics of Southeast Asia: Journal of Geophysical Research, v. 98, p. 6299–6328. doi:10.1029/92JB02280

Canales, J.P., Ito, G., Detrick, R.S., and Sinton, J., 2002, Crustal thickness along the western Galapagos Spreading Center and the compensation of the Galapagos hotspot swell: Earth and Planetary Science Letters, v. 203, p. 311–327. doi:10.1016/S0012-821X(02)00843-9

Cande, S.C., and Kent, D.V., 1995, Revised calibration of the geomagnetic polarity timescale for the Late Cretaceous and Cenozoic: Journal of Geophysical Research, v. 100, p. 6093–6095. doi:10.1029/94JB03098

Chen, B., and Lei, S., 1987, Map of crustal structures, *in* He, L., and Chen, B., eds., Atlas of geology and geophysics of South China Sea: China, Map Publishing House of Guangdong Province, p. 10.

Cowie, P.A., and Karner, G.D., 1990, Gravity effect of sediment compaction: Examples from the North-Sea and the Rhine Graben: Earth and Planetary Science Letters, v. 99, p. 141–153. doi:10.1016/0012-821X(90)90078-C

Ding, W.W., and Li, J.B., 2016, Propagated rifting in the Southwest Sub-basin, South China Sea: Insights from analogue modeling: Journal of Geodynamics, v. 17, p. 71–86. doi:10.1016/j.jog.2016.02.004

Ding, W.W., Li, J.B., and Clift, P., 2016, Spreading dynamics and sedimentary process of the Southwest-Sub-basin, South China Sea: Constraints from multi-channel seismic data and IODP Expedition 349: Journal of Asian Earth Sciences, v. 115, p. 97–113. doi:10.1016/j.jseaes.2015.09.013

Divins, D.L., 2003, NGDC total sediment thickness of the World's oceans & marginal seas; http://www.ngdc.noaa.gov/mgg/sedthick/sedthick.html (Accessed 2016).

Flower, M.F.J., Zhang, M., Chen, C.Y., Tu, K., and Xie, G., 1992, Magmatism in the South China basin: 2. post-spreading quaternary basalts from Hainan Island, South China: Chemical Geology, v. 97, p. 65–87. doi:10.1016/0009-2541(92)90136-S

Forsyth, D.W., 1993, Crustal thickness and the average depth and degree of melting in fractional melting models of passive flow beneath mid-ocean ridges: Journal of Geophysical Research, v. 981, p. 16073–16079. doi:10.1029/93JB01722

Gradstein, F.M., Agterberg, F.P., Ogg, J.G., Hardenbol, J., Veen, P., Thierry, J., and Huang, Z., 1993, A Mesozoic time scale: Journal of Geophysical Research, v. 99, p. 24051–24074. doi:10.1029/94JB01889

Gradstein, F.M., Ogg, J.G., Schmitz, M.D., and Ogg, G.M., 2012, The geologic time scale 2012: Boston, MA, Elsevier, 1176 pp.

Gregg, P.M., Behn, M.D., Lin, J., and Grove, T.L., 2009, Melt generation, crystallization, and extraction beneath segmented oceanic transform faults: Journal of Geophysical Research, v. 114, p. 292–310. doi:10.1029/2008JB006100

Hayes, D.E., and Nissen, S.S., 2005, The South China Sea margins: Implications for rifting contrasts: Earth and Planetary Science Letters, v. 237, p. 601–616. doi:10.1016/j.epsl.2005.06.017

He, E., Zhao, M., Qiu, X., Sibuet, J.C., Wang, J., and Zhang, J., 2016, Crustal structure across the post-spreading magmatic ridge of the East Sub-basin in the South China Sea: Tectonic significance: Journal of Asian Earth Sciences, v. 121, p. 139–152. doi:10.1016/j.jseaes.2016.03.003

Huang, H., Tosi, N., Chang, S., Xia, S., and Qiu, X., 2016, Receiver function imaging of the mantle transition zone beneath the South China block: Geochemistry Geophysics Geosystems, v. 16, p. 3666–3678. doi:10.1002/2015GC005978

Koppers, A., 2014, On the 40Ar/39Ar dating of low-potassium ocean crust basalt from IODP Expedition 349, South China Sea (abstract): AGU Fall Meeting, San Francisco, USA.

Kuo, B.Y., and Forsyth, D.W., 1988, Gravity anomalies of the ridge-transform system in the South Atlantic between 31 and 34.5°S: Upwelling centers and variations in crustal thickness: Marine Geophysical Research, v. 10, p. 205–232. doi:10.1007/BF00310065

Li, C., Li, J., Ding, W., Franke, D., Yao, Y., Shi, H., et al., 2015, Seismic stratigraphy of the central South China Sea basin and implications for neotectonics: Journal of Geophysical Research, v. 120, p. 1377–1399.

Li, C., and Song, T., 2012, Magnetic anomalies of the oceanic crust and the deep evolution of the Cenozoic oceanic crust in the South China Sea: Science Bulletin, v. 57, p. 1879–1895. [In Chinese.]

Li, C., Xu, X., Lin, J., Sun, Z., Zhu, J., Yao, Y., Zhao, X., Liu, Q., Kulhanek, D.K., Wang, J., Song, T., Zhao, J., Qiu, N., Guan, Y., Zhou, Z., Williams, T., Bao, R., Briais, A., Brown, E.A., Chen, Y., Clift, P.D., Colwell, F.S., Dadd, K.A., Ding, W., Almeida, I.H., Huang, X.-L., Hyun, S., Jiang, T., Koppers, A.A.P., Li, Q., Liu, C., Liu, Z., Nagai, R.H., Peleo-Alampay, A., Su, X., Tejada, M.L.G., Trinh, H.S., Yeh, Y.-C., Zhang, C., Zhang, F., and Zhang, G.-L., 2014, Ages and magnetic structures of the South China Sea constrained by deep tow magnetic surveys and IODP Expedition 349: Geochemistry, Geophysics, Geosystems, v. 15, p. 4958–4983. doi:10.1002/2014GC005567

Li, S., Meng, X., Guo, L., and Yao, C., 2012, Characteristics of gravity anomalies in the South China Sea and their tectonic implications: Geoscience, v. 26, p. 1154–1161. [In Chinese.]

Lin, J., Purdy, G.M., Schouten, H., Sempere, J.C., and Zervas, C., 1990, Evidence from gravity data for focused magmatic accretion along the Mid-Atlantic Ridge: Nature, v. 344, p. 627–632. doi:10.1038/344627a0

Liu, Z., Wang, Q., Yuan, H., and Su, D., 1985, The Bouguer anomalies and depths of Mohorovicic discontinuity in the South China Sea region: Acta Oceanologica Sinica, v. 4, p. 579–590.

Ludwig, W.J., Kumar, N., and Houtz, R.E., 1979, Profiler-sonobuoy measurements in the South China Sea Basin: Journal of Geophysical Research, v. 84, p. 3505–3518. doi:10.1029/JB084iB07p03505

Lv, C., Hao, T., Qiu, X., Zhao, M., and You, Q., 2011, Deep crustal structure of the northern part of Southwest Subbasin, South China Sea, from ocean bottom seismic data: Chinese Journal of Geophysics, v. 54, p. 3117–3126. [In Chinese.]

Magde, L.S., and Detrick, R.S., 1995, Crustal and upper mantle contribution to the axial gravity anomaly at the southern East Pacific Rise: Journal of Geophysical Research, v. 100, p. 3747–3766. doi:10.1029/94JB02869

Magde, L.S., and Sparks, D.W., 1997, Three-dimensional mantle upwelling, melt generation, and melt migration beneath segment slow spreading ridges: Journal of Geophysical Research, v. 102, p. 20571–20583. doi:10.1029/97JB01278

Magde, L.S., Sparks, D.W., and Detrick, R.S., 1997, The relationship between buoyant mantle flow, melt migration, and gravity bull's eyes at the Mid-Atlantic Ridge between 33°N and 35°N: Earth and Planetary Science Letters, v. 148, p. 59–67. doi:10.1016/S0012-821X(97)00039-3

Marks, K.M., 1996, Resolution of the Scripps/NOAA marine gravity field from satellite altimetry: Geophysical Research Letters, v. 23, p. 2069–2072. doi:10.1029/96GL02059

Müller, R.D., Sdrolias, M., Gaina, C., and Roest, W.R., 2008, Age, spreading rates, and spreading asymmetry of the world's ocean crust: Geochemistry, Geophysics, Geosystems, v. 9, p. Q04006. doi:10.1029/2007GC001743

Neumann, G.A., Forsyth, D.W., and Sandwell, D., 1993, Comparison of marine gravity from shipboard and high-density satellite altimetry along the Mid-Atlantic Ridge, 30.5°-35.5° S: Geophysical Research Letters, v. 20, p. 1639–1642. doi:10.1029/93GL01487

Parker, R.L., 1973, The rapid calculation of potential anomalies: Geophysical Journal of the Royal Astronomical Society, v. 31, p. 447–455. doi:10.1111/j.1365-246X.1973.tb06513.x

Qiu, X., Ye, S., Wu, S., Shi, X., Zhou, D., Xia, K., and Flueh, E.R., 2001, Crustal structure across the Xisha trough, northwestern South China Sea: Tectonophysics, v. 341, p. 179–193. doi:10.1016/S0040-1951(01)00222-0

Qiu, X., Zhao, M., Ao, W., Lv, C., Hao, T., You, Q., Ruan, A.-G., and Li, J.-B., 2011, OBS survey and crustal structure of the SW Subbasin and Nansha Block, South China Sea: Chinese Journal of Geophysics, v. 54, p. 1009–1021. doi:10.1002/cjg2.v54.6

Ruan, A., Niu, X., Qiu, X., Li, J., Wu, Z., Zhao, M., and Wei, X., 2011, A wide angle ocean botttom seismometer profile across Liyue Bank, the southern margin of South China Sea: Chinese Journal of Geophysics, v. 54, p. 3139–3149. [In Chinese.]

Ruan, A., Wei, X., Niu, X., Zhang, J., Dong, C., Wu, Z., and Wang, X., 2016, Crustal structure and fracture zone in the central basin of the South China Sea from wide angle seismic experiments using obs: Tectonophysics, v. 688, p. 1–10. doi:10.1016/j.tecto.2016.09.022

Sandwell, D.T., Müller, R.D., Smith, W.H., Garcia, E., and Francis, R., 2014, New global marine gravity model from CryoSat-2 and Jason-1 reveals buried tectonic structure: Science, v. 346, p. 65–67. doi:10.1126/science.1258213

Smith, W.H.F., and Sandwell, D.T., 1997, Global sea floor topography from satellite altimetry and ship depth soundings: Science, v. 277, p. 1956–1962. doi:10.1126/science.277.5334.1956

Song, T., and Li, C., 2012, The opening ages and mode of the South China Sea estimated from high-density magnetic tracks: Progress in Geophysics, v. 27, p. 1432–1442. [In Chinese.]

Sparks, D.W., and Parmentier, E., 1991, Melt extraction from the mantle beneath spreading centers: Earth and Planetary Science Letters, v. 105, p. 368–377. doi:10.1016/0012-821X(91)90178-K

Sparks, D.W., Parmentier, E., and Morgan, J.P., 1993, Three-dimensional mantle convection beneath a segmented spreading center: Implications for along-axis variations in crustal thickness and gravity: Journal of Geophysical Research, v. 98, p. 21977–21995. doi:10.1029/93JB02397

Taylor, B., and Hayes, D.E., 1980, The tectonic evolution of the South China Sea Basin, *in* Hayes, D.E., ed., The tectonic and geologic evolution of Southeast Asian Seas and Islands: AGU Geophysical Monograph, American Geophysical Union, Washington, D. C., Volume 23, p. 89–104.

Taylor, B., and Hayes, D.E., 1983, Origin and history of the South China Sea Basin, *in* Hayes, D.E., ed., The tectonic and geologic evolution of Southeast Asian Seas and Islands, Part 2: AGU geophysical monograph, American Geophysical Union, Washington, D. C., Volume 27, p. 23–56.

Trung, N., Lee, S., and Que, B., 2004, Satellite gravity anomalies and their correlation with the major tectonic features in the South China Sea: Gondwana Research, v. 7, p. 407–424. doi:10.1016/S1342-937X(05)70793-0

Turcotte, D.L., and Schubert, G., 2002, Geodynamics (2nd edition): Cambridge University Press, Cambridge, UK, p. 472.

Wang, T.K., Chen, M.K., Lee, C.S., and Xia, K., 2006, Seismic imaging of the transitional crust across the northeastern margin of the South China Sea: Tectonophysics, v. 412, p. 237–254. doi:10.1016/j.tecto.2005.10.039

Wang, Y., Hang, X., Luo, Z., Qiu, Z., Ding, W., and Li, J., 2009, Late Miocene magmatism and evolution of Zhenbei-Huangyan Seamount in the South China Sea: Evidence from petrochemistry and chronology: Acta Oceanologica Sinica, v. 31, p. 93–102. [In Chinese.]

Wei, S., and Chen, Y.J., 2016, Seismic evidence of the Hainan mantle plume by receiver function analysis in southern China: Geophysical Research Letters, v. 43, p. 8978–8985. doi:10.1002/2016GL069513

Wei, X., Ruan, A., Zhao, M., Qiu, X., Li, J., Zhu, J., Wu, Z., and Ding, W., 2011, A wide-angle OBS profile across Dongsha Uplift and Chaoshan Depression in the mid-northern South China Sea: Chinese Journal of Geophysics, v. 54, p. 3325–3335.

Wilson, J.T., 1966, Did the Atlantic close and then re-open?: Nature, v. 211, p. 676–681. doi:10.1038/211676a0

Workman, R.K., and Hart, S.R., 2005, Major and trace element composition of the depleted MORB mantle (DMM): Earth and Planetary Science Letters, v. 231, p. 53–72. doi:10.1016/j.epsl.2004.12.005

Wu, Z., Li, J., Ruan, A., Lou, H., Ding, W., Niu, X., and Li, X., 2011, Crustal structure of the northwestern sub-basin, South China Sea: Results from a wide-angle seismic experiment: Science in China, Earth Science, v. 41, p. 1463–1476.

Xia, S., Zhao, D., Sun, J., and Huang, H., 2016, Teleseismic imaging of the mantle beneath southernmost china: New insights into the Hainan plume: Gondwana Research, v. 36, p. 46–56. doi:10.1016/j.gr.2016.05.003

Xu, H., Ma, H., Song, H., and Chen, A., 2011, Eastern South China Sea basin expansion numerical modeling: Chinese Journal of Geophysics, v. 54, p. 956–966. doi:10.1002/cjg2.1676

Xu, Y., Wei, J., Qiu, H., Zhang, H., and Huang, X., 2012, Opening and evolution of the South China Sea constrained by studies on volcanic rocks. Preliminary results and a research design: Science Bulletin, v. 57, p. 1863–1878.

Yan, P., Zhou, D., and Liu, Z., 2001, A crustal structure profile across the northern continental margin of the South China Sea: Tectonophysics, v. 338, p. 1–21. doi:10.1016/S0040-1951(01)00062-2

Yan, Q., 2007, Hainan mantle plume and the formation and evolution of the South China Sea: Geological Journal of China Universities, v. 13, p. 311–322.

Yan, Q., Castillo, P., Shi, X., Wang, L., Liao, L., and Ren, J., 2015, Geochemistry and petrogenesis of volcanic rocks from Daimao Seamount (South China Sea) and their tectonic implications: Lithos, v. 218, p. 117–126. doi:10.1016/j.lithos.2014.12.023

Yan, Q., Shi, X., Wang, K., Bu, W., and Xiao, L., 2008, Major element, trace element, and Sr, Nd and Pb isotope studies

of Cenozoic basalts from the South China Sea, Science China: Earth Sciences, v. 51, p. 550–566.

Yang., S., Qiu, Y., and Zhu, B., 2015, Atlas of geology and geophysics of the South China Sea: China Navigation Publications. Tianjin, China, p. 9.

Zhang, J., Li, J., Ruan, A., Wu, Z., Yu, Z., Niu, X., and Ding, W., 2016, The velocity structure of a fossil spreading centre in the southwest sub-basin, South China Sea: Geological Journal, v. 51, p. 548–561. doi:10.1002/gj.v51.S1

Zhao, M., Qiu, X., Xia, S., Xu, H., Wang, P., Wang, T.K., Lee, C.-S., and Xia, K., 2010, Seismic structure in the northeastern South China Sea: S-wave velocity and *Vp/Vs* ratios derived from three-component OBS data: Tectonophysics, v. 480, p. 183–197. doi:10.1016/j.tecto.2009.10.004

Zhou, L., Liu, F., Zhang, J., and Chen, X., 2005, Determination of the crustal velocity model of Dongsha islands using the inversion of τ-p wave field: Progress in Geophysics, v. 20, p. 503–506. [In Chinese.]